Journal of Materials Chemistry A

ROYAL SOCIETY OF CHEMISTRY

PAPER

View Article Online
View Journal

Cite this: DOI: 10.1039/d5ta04960a

A solvothermal approach to nano-designing M-N-H systems: unveiling new pathways to dimensional control in the lithium nitride hydride ammonia synthesis catalyst

Fatima M. Abi-Ghaida* and Joshua W. Makepeace

Received 19th June 2025
Accepted 5th September 2025

DOI: 10.1039/d5ta04960a

rsc.li/materials-a

The Li–N–H system spans a rich network of reactive phases that encompass Li_3N – Li_4NH – Li_2NH – $LiNH_2$ – LiH, interconnected through a number of solid solutions and mediated *via* NH_3, H_2, and/or N_2 exchange. Realizing the full potential of these Li–N–H systems in ammonia catalysis and hydrogen storage applications has been hindered by the inability to 'nano-design' them beyond conventional bulk synthesis. Here, we present a novel solvothermal route for the synthesis and nanostructurisation of Li–N–H and Li–Na–N–H materials, providing a solution-phase route to these air-sensitive and reactive materials. The method enables enhanced morphological and dimensional control compared to solid-state routes, yielding nanostructures such as wires, rods, and particles with characteristic sizes from 300 to 900 nm. We systematically explore the structural and microstructural evolution of these phases, and demonstrate the influence of mineralisers on the sample morphology. We report evidence of enhanced nitrogen activation, air-stability and ammonia synthesis activity for these samples, balanced against their propensity for carbon contamination. This work opens the possibility of a significantly expanded synthesis approaches to Li–N–H materials, and M-N-H materials more broadly.

Introduction

Materials engineering, particularly the design of quantum nanomaterials, plays a fundamental role in advancing sustainable, self-sufficient, and economical energy technologies. However, the development of next-generation nanomaterials is often constrained by the limited tunability of conventional solid-state synthetic routes. This lack of flexibility becomes especially pronounced when dealing with highly reactive and metastable inorganic systems such as metal hydrides, amides, imides and nitride hydrides (collectively, Group I and II M-N-H materials), where established nano-design and nanostructuring techniques frequently fall short as opposed to the versatile, and stable chemistries of their organic or hybrid counterparts.[1,2]

Despite the relative simplicity and scalability of conventional solid-state (SS) approaches for bulk M-N-H materials, they suffer from unfavorable reaction conditions, inflexible pathways, low surface area, poor particle dispersion, microstructural defects, and destabilization of highly active phases. These limitations are felt particularly keenly given the rising relevance of M-N-H materials in applications such as reversible hydrogen storage,[3] promotion of ammonia synthesis and decomposition,[4–8] and efficient solid-state electrolytes.[9,10] In principle, their efficacy relies on interfacial and surface-mediated processes that would undoubtedly benefit from controlled nano-scaling and uniform morphology.

Nanomaterials, by contrast, not only retain but often transcend the fundamental properties of their bulk analogues, revealing quantum phenomena that stem from precise control over dimensionality, composition, and architecture. This is typically achieved *via* unconventional synthetic protocols such as solvothermal/hydrothermal routes,[11–13] sol–gel chemistry,[14] colloidal synthesis, and modulated nucleation and growth,[15,16] *etc.* Among the clearest demonstrations of these advantages are nanostructured metal hydrides, which display improved hydrogen sorption kinetics, tunable thermodynamic properties, and enhanced cycling stability compared to their bulk counterparts particularly upon unlocking their quantum confinement effects.[17] Such nano-design methodologies have yet to be profoundly explored in M-N-H materials such as the Li–N–H system, where very few examples of nanostructured materials currently exist, largely due to the severe reactivity, basicity, and insolubility of lithium-based precursors (such as lithium nitride (Li_3N), lithium hydride (LiH) and lithium amide ($LiNH_2$)). Despite their limitations, these systems are central to the production of lithium-ion batteries,[18] lithium solid-state electrolytes,[9,19] hydrogen storage materials,[20,21] and catalysts for sustainable fuel production.[22]

The compositional and structural versatility of Li–N–H family spans the lithium amide (NH_2^-) – imide (NH^{2-}) – nitride hydride (N^{3-}, H^-) phase space.[23] The seamless interconversion

School of Chemistry, University of Birmingham, Edgbaston, B15 2TT, UK. E-mail: f.abighaida@bham.ac.uk; j.w.makepeace@bham.ac.uk

between these phases through solid solutions (amide–imide and imide–nitride–hydride, chiefly) is one of the most critical features of its fast-ion conduction, reversible hydrogen storage and effective ammonia catalysis.[21] For instance, the Li–N–H system has been established as a critical platform in solid-state hydrogen storage; with reversible hydrogen content facilitated by these solid solutions (eqn (1) and (2)).[3,24]

$$Li_3N + H_2 \rightarrow Li_2NH + LiH \text{ (\textit{via} nitride–hydride–imide)} \quad (1)$$

$$Li_2NH + H_2 \rightarrow LiNH_2 + LiH \text{ (\textit{via} imide–amide)} \quad (2)$$

Efforts to optimize the thermodynamics and kinetics of the Li–N–H system have alluded to the importance of nano-designing. That is, there remains a critical unmet need to build such Li-based materials through bottom-up and tunable approaches that can firstly control morphology, dimensionality, and surface area and ultimately access quantum phenomena such as facet-selective confinement and interfacial reactivity.[7,25,26]

Tapia-Ruiz *et al.* provided one amongst very few reported approaches for designing one- and two-dimensional nanostructures of Li_3N. The authors achieved the nanostructurisation of Li_3N in the vicinity of the ambient decomposition temperature of Li_3N (815 °C) under reduced pressure and rationalized the mechanism *via* the decomposition of Li_3N into Li seeds that would serve as nucleation sites for the uptake of N_2 species. This led to a supersaturated Li-environment and sequential anisotropic growth of lithium into Li_3N nanofibers.[27] Undeniably, Li_3N nanofibers could prove crucial for hydrogen storage and fast Li-ion conduction, but such synthesis protocols necessitate extremely low pressure and high temperature conditions. Additional examples include reactions performed under supercritical ammonia (ammonothermal methods) used to isolate single-crystals of lithium-containing amides as $Li[Sn(NH_2)_3]$, $KLi_3(NH_2)_4$ and $Li_3Na(NH_2)_4$,[28–30] but often rely on extreme ammonia pressures (>1 kbar) in specialized reaction vessels, limiting their broader applicability and scalability.

Herein, we demonstrate the nano-design of Li–N–H materials *via* a simple solvothermal route. This strategy provides access to lithium nitride hydride, lithium imide, and non-stoichiometric mixed alkali-metal phases, synthesized from commercially available and scalable Li_3N, LiH, and $NaNH_2$ precursors under moderate temperatures and autogenous pressures. The synthetic route offers tunable morphology, compositional versatility, and the potential for *in situ* incorporation of catalytically active moieties,[31] thus opening a new direction for Li–N–H materials in hydrogen storage and catalysis.

Results and discussion

Solvothermal synthesis of lithium nitride hydride *via* Li_3N and LiH

Phase chemistry and crystallography. Lithium nitride hydride (Li_4NH) was initially reported in the late 1990s by Marx *et al.*[32] through solid-state approaches (eqn (3)).[33] Recently, the material has been highlighted as an effective chemical looping ammonia synthesis agent,[25] where solid solutions with lithium imide ($Li_{4-2x}N_{1-x}H_{1-x}(NH)_x$ or simply $Li_{2+x}NH$) (eqn (4)), have been implicated as the active phase in ammonia synthesis processes.[34]

$$Li_3N + LiH \rightarrow Li_4NH \quad (3)$$

$$(2 - x)Li_2NH + xLi_4NH \rightarrow Li_{4-2x}N_{1-x}H_{1-x}(NH)_x \quad (4)$$

The solvothermal synthesis of Li_4NH was effectuated starting from the ball-milling of commercially available lithium precursors, Li_3N and LiH, prior to dispersion in aprotic anhydrous solvents (benzene, toluene, dioxane, and tetrahydrofuran (THF)), the resulting suspension was stirred, transferred to a PTFE insert under an argon atmosphere and subjected to solvothermal reactions at variable temperatures (175–275 °C) and relatively comparable pressures and concentrations. Though benzene displayed lower oxidation byproducts, discussion will mainly center on the samples synthesized in toluene due to its reduced hazard potential compared to benzene, as well as its more agreeable environmental and sustainability profiles. Notably, the use of anhydrous cyclic ethers as solvents was unfavorable as samples prepared in THF and dioxane displayed higher oxide percentages.

The powder X-ray diffraction (PXRD) data of the products of these reactions reveal the broad success of the solvothermal method in that the Li_4NH has been synthesized *via* this novel approach at 275 °C (Fig. 1A) along with an $Fm\bar{3}m$ solid solution phase (Fig. 1B). The indexed Bragg peaks of Li_4NH at 275 °C are consistent with that of the tetragonal space group $I4_1/a$ with lattice parameters $a = 4.8920(1)$, $c = 9.9320(4)$ Å and are comparable with the lattice parameters seen in SS synthesis of Li_4NH at 520 °C ($a = 4.8908(3)$, $c = 9.9274(7)$ Å, Fig. SI-1). Although the unit cell of Li_4NH is more accurately depicted as an anti-Scheelite structure, it can be described as a $a \times a \times 2a$ face-centered cubic (fcc) structure, with two anti-fluorite unit cells where N^{3-} and H^- ions sit on the core fcc lattice points and are ordered along the c axis of the doubled fcc cell, while Li^+ ions sit close to the face of the tetrahedral holes. This correlation to the antifluorite structure also held by Li_2NH helps to illustrate why cubic $Li_{2+x}NH$ solid solutions form when imide groups (NH^{2-}) are partially substituted into Li_4NH. Indeed, XRD patterns depict the appearance of the cubic $Fm\bar{3}m$ phase with lattice parameter $a = 4.9688(3)$ Å consistent with a disordered imide–nitride–hydride $Li_{2+x}NH$ solid solution where Rietveld refinement projects x to span an interval of 0.82 to 0.88 ($Li_{3.64}NH$ to $Li_{3.72}NH$).[35] Increasing the reaction time consistently by 12 hours increments causes a significant increase in the $Fm\bar{3}m$ solid solution phase accompanied by a relative decrease in the tetragonal Li_4NH phase. The formation and evolution of this cubic phase throughout the solvothermal system can be partially attributed to compositional variations evident not only in the initial 12 hours reaction, as noted from the appearance of 2.37 wt% of Li_2O (Fig. 1B) which disrupts the overall stoichiometry of the mixture, but potentially as a result

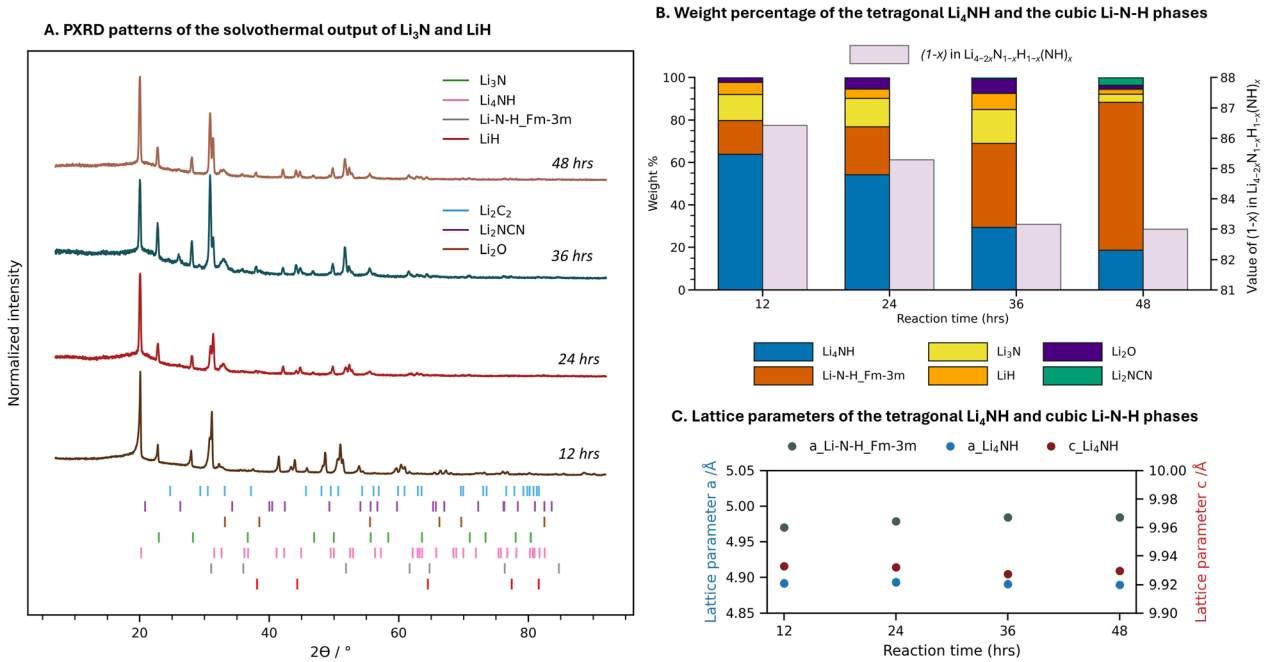

Fig. 1 (A) PXRD patterns of the solvothermal output of Li_3N and LiH at 275 °C as a factor of time (B) weight percentage correlation of the tetragonal Li_4NH and the cubic $Fm\bar{3}m$ phases depicting an inverse relationship *versus* time where a gradual decrease in the weight percentage of the tetragonal phase and an increase in the weight percentage of the cubic $Li_{4-2x}N_{1-x}H_{1-x}(NH)_x$ solid solution is noted (C) lattice parameters of the tetragonal Li_4NH and cubic Li–N–H phases.

of the strenuous conditions exerted on Li_4NH within the vessel. Moreover, carbon, resulting from solvent decomposition, induces side reactions resulting in the formation of traces of lithium carbodiimide or dicyanamide (Li_2NCN) and lithium carbide (Li_2C_2) which further interrupts the composition and therefore the structural ordering of the system; the two side products can also be noted to significantly increase upon prolonged heating of the reaction mixture (Fig. 1A, at 36 hours) and dominate upon temperature increase above 300 °C. Further refinement of the PXRD across 12 to 48 hours indicates a decrease in the tetragonal phase and an increase in the cubic phase which exhibits a slight decrease in the nitride hydride character and a correlated increase in the NH^{2-} character (Fig. 1B) suggesting the presence of a complex and interchangeable pathway amongst the nitride hydride and imide moieties which is likely mediated by the *in situ* release and uptake of N_2 and H_2.[36] This phenomenon was substantiated when a SS synthesized sample comprising only the tetragonal Li_4NH was subjected to solvothermal treatment at 275 °C and displayed the formation of the cubic phase; that is, the 12 hours solvothermally treated $I4_1/a$ Li_4NH exhibits the appearance of 26 wt% of the $Fm\bar{3}m$ phase alluding to the partial dissolution of tetragonal Li_4NH and its reprecipitation as the cubic $Fm\bar{3}m$ phase (Fig. SI-2).

In a solid-state reaction, the mechanism of Li_4NH synthesis suggests that the $Fm\bar{3}m$ Li–N–H phase plays the role of a conduit (transition-state solid solution) that ensures the recombination or homogenous assimilation of the chemical moieties which then reorganizes into Li_4NH if compositional and structural ordering has been established. However, within a solvothermal

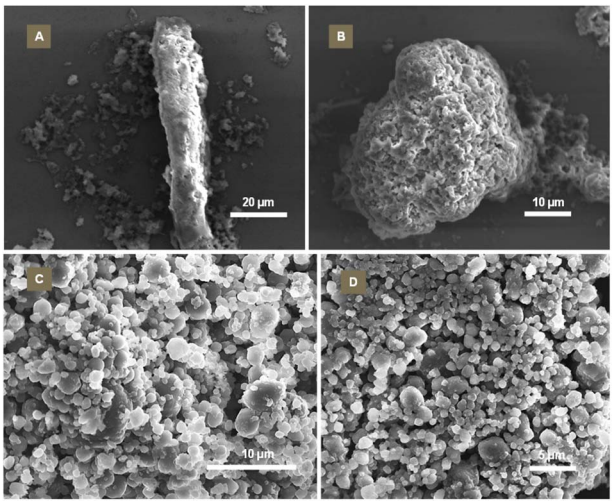

Fig. 2 Scanning electron microscopy images of (A) Li_4NH synthesized *via* conventional solid-state thermal approaches displaying irregular and non-uniform distribution of shapes and sizes, (B) ball-milled Li_4NH after solid-state thermal synthesis, (C) Li–N–H synthesized *via* novel solvothermal route displaying a relatively uniform distribution of nanoparticles shapes and sizes as well as coalesced aggregates and particle agglomerates in benzene, and (D) in toluene attributed to surface energy and electrostatic interactions; note that standard particle dispersion and deposition techniques were investigated but deemed inadequate as the morphology and extent of aggregation were notably different.

medium, trace Li_2O, carbon contamination and Li_2NCN introduce compositional heterogeneity where Li_4NH dissolves back into the solution and reprecipitates as defect-tolerant cubic

$Fm\bar{3}m$ $Li_{2+x}NH$ solid solution. This is evident from the inversely correlated weight percentages of Li_4NH and $Fm\bar{3}m$ phase with reaction time in Fig. 1B. This reconstructive dissolution–reprecipitation cycle, driven by the cubic phase's capacity to accommodate non-stoichiometry, gradually converts the $I4_1/a$ material to the $Fm\bar{3}m$ phase where the lattice parameters and cell volume depict a gradual increase with time associated with structural expansion to accommodate a mixture of N^{3-}, H^-, and NH^{2-} anions (Fig. 1C).

Raman spectroscopy investigations of the solvothermally synthesized tetragonal Li_4NH displayed its characteristic peaks at low wavenumbers corresponding to phonon modes of the nitride hydride moieties (*ca.* 455, 588, and 780 cm^{-1}), along with a small broad peak at *ca.* 3165 cm^{-1} attributed to N–H stretching of the NH^{2-} moiety (Fig. SI-3).[37]

Sample morphology. Of critical importance to this study is the impact of solvothermal conditions on the morphology of the samples. Scanning electron microscopy (SEM) images of these solvothermal phases (Fig. 2C and D) display a semi-uniform distribution of smaller particle sizes (300–600 nm) interrupted by coalesced aggregates of 900 nm to 1.5 μm likely due to strong electrostatic interactions; this is to be expected as this work aims to establish the preliminary synthesis of these materials without stabilizing agents (SAs) or structure directing agents (SDAs). Herein, we also note that the degree of aggregation observed in Fig. 2C and D may be influenced by the dry deposition method used.

Though SDAs have not been incorporated into the reaction system, the morphology of the solvothermal Li–N–H materials differs drastically from that of the SS synthesized samples (Fig. 2A and B), and depicts polyhedral quasi-spherical nanoparticles featuring low aspect ratios and evidence an improvement in the morphological and surface area-to-volume control obtained from a solvothermal system compared with the irregular morphology and large particle sizes of SS synthesized Li_4NH samples. This emphasizes the potential for solvothermal approaches to deliver higher surface areas and greater morphological control. Moreover, the subtle differences in product morphology between reactions conducted in benzene and toluene (Fig. 2C and D, respectively) highlight the influence of solvent environment on crystal growth behavior. Although toluene exhibits a slightly higher solvation capacity, both benzene and toluene possess low dielectric constants and limited ability to solvate ionic precursors effectively. Nevertheless, toluene's dipolar character offers marginally improved stabilization of polarizable ionic intermediates, potentially enhancing precursor dispersion and modulating local polarization effects during solvothermal synthesis. This enhanced stabilization increases the frequency of nucleation sites and moderates subsequent growth kinetics, which translates into smaller, more uniform particle morphologies relative to benzene.

Despite these subtle differences, dimensional control in both solvent systems remains partial, suggesting that existing solvent effects alone do not fully dictate morphology. In this model, we hypothesize that nucleation and crystal growth proceed through a continuous dissolution–reprecipitation mechanism driven by local supersaturation within the sealed vessel. Interfacial release of reactive ionic species from partially soluble precursors facilitates the nucleation of ordered domains, while limited solvent coordination and low ionic solubility restrict anisotropic growth, leading to the observed morphology. That is, both Li_3N and LiH generate transient Li^+, N^{3-}, and H^- species at the solid–liquid interface where local supersaturation near reactive zones promotes heterogeneous nucleation of the tetragonal $I4_1/a$ Li_4NH on residual precursor surfaces while nascent Li_4NH nuclei, possessing high surface energy, rapidly grow by ion flux from the surrounding medium, yielding quasi-spherical particles. The high surface energy of these Li–N–H nuclei and the absence of surface capping agents prompt Ostwald ripening and rapid coalescence, further supporting the observed morphology of quasi-spherical particles and their aggregation tendencies.

Impact on functional properties. A key motivation for the development of this approach was to enhance the functional properties of the materials in question. In this case, lithium nitride–hydride has two key parameters to consider: its sensitivity to air and potential enhancements to its ability to synthesise ammonia at lower temperatures.

The air stability of solvothermally prepared lithium nitride–hydride was evaluated against its solid-state analogue by time-resolved XRD of powders exposed to air over 48 h. Contour plots of the diffraction data and refined phase fractions are provided in Supplementary Fig SI-4 to SI-6. The solvothermal sample exhibits a slower decline in the combined Li–N–H (Li_4NH, Li_3N, LiH and Li_2NH) phase fractions for each sample shown in Fig. 3 indicating a modest enhancement in air stability compared to the solid-state material. Notably, given that the smaller particle size of the solvothermal product would typically promote faster oxidation through enhanced gas–solid interactions, the observed stability instead suggests potential passivation of the Li_4NH surface, likely mediated by the carbon contamination described above.

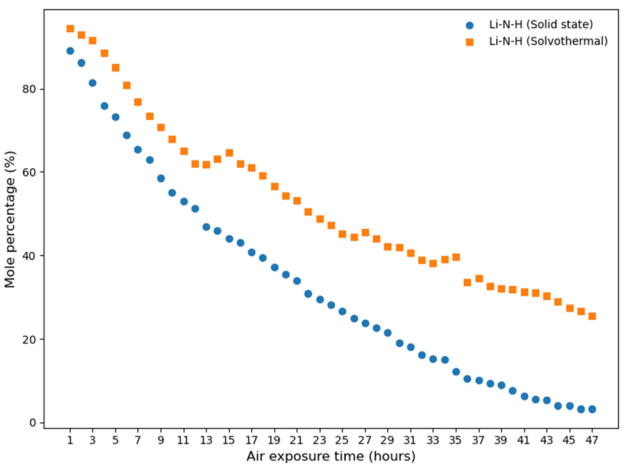

Fig. 3 The combined Li–N–H molar percentage of samples prepared by solid state and solvothermal synthesis as a function of air-exposure time.

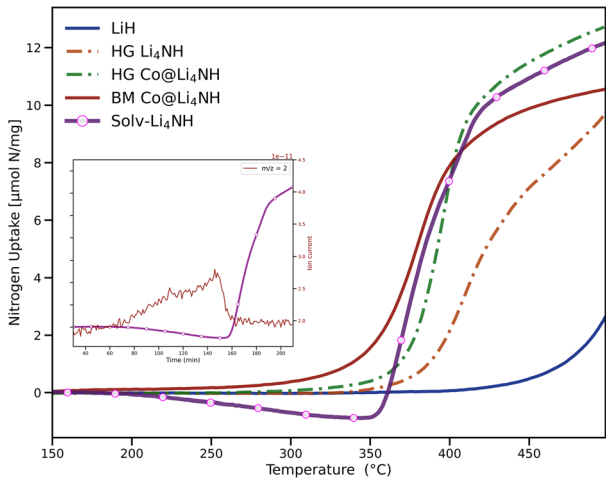

Fig. 4 N_2 uptake profiles as measured in a TPR experiment (ramp to 520 °C at 2.5 °C min^{-1} followed by 60 min isothermal segment) of LiH, the solid-state synthesized Li_4NH (HG Li_4NH), 20 wt% Co@Li_4NH, and the solvothermal sample prepared in toluene (Solv-Li_4NH). HG = hand-ground, BM = ball-milled.

Nitrogen uptake measurements are a critical measure of the ammonia synthesis properties, particularly in chemical looping ammonia synthesis where reaction with N_2 is one half of the overall reaction, and is reported in comparison with other relevant materials in Fig. 4. The N_2 uptake behaviour of the solvothermal Li_4NH, investigated up to 520 °C, displays an initial mass loss between 225 and 345 °C accompanied by gradual hydrogen evolution consistent with Li_2NCN formation arising from carbon contamination (Fig. 4, inset). N_2 uptake of the Solv-Li_4NH sample begins at a lower onset temperature of 350 °C compared to solid-state synthesized and hand-ground Li_4NH (HG-Li_4NH), which starts reacting around 400 °C while LiH shows N_2 uptake onset at 450 °C. In fact, the gain in surface area and morphology in Solv-Li_4NH induces comparable uptake kinetics to that of cobalt-composited Li_4NH (Fig. 4) which similarly shows intermediate onset temperatures near 350 °C (Co@Li_4NH composites, prepared by hand grinding or ball milling of solid-state synthesized Li_4NH with 20 wt% of Co). Moreover, Solv-Li_4NH fixes significantly more nitrogen per unit mass and per mol of Li compared to solid-state and composited analogues. This superior performance persists despite partial deactivation from irreversible Li_2NCN formation (23 wt% of cyanamide in Li_2NCN@Li_4NH), demonstrating the improved nitrogen-fixing efficiency of the solvothermal route and affirming its advantage for ammonia synthesis applications.

Rietveld refinement of the post-N_2 uptake PXRD pattern displays the presence of the $Fm\bar{3}m$ phase (65.4 wt%), as well as Li_2NCN (23.2 wt%) arising from carbon contamination (estimated at 6 wt%) and Li_2O (11.4 wt% arising from transport) (Fig. SI-7). That is, when Li_4NH reacts with nitrogen, it forms an imide $Fm\bar{3}m$ structure with a lattice parameter of $a = 5.0721(1)$ Å. Hydrogen and ammonia were not detected during the N_2-uptake stage indicating that the reaction does not produce volatile byproducts (H_2 was only detected during Li_2NCN formation). The $Fm\bar{3}m$ phase exhibits a slightly increased lattice parameter than the solvothermal $Fm\bar{3}m$ phase ($a = 4.963876(9)$ Å) which suggests that nitrogen fixation in Li_4NH does not result in the formation of the stoichiometric $Fd\bar{3}m$ Li_2NH, but an imide-rich solid solution.

Given the encouraging nitrogen uptake data, 30 mg of three catalysts (Solv-Li_4NH, HG-Li_4NH, BM-Li_4NH), were loaded into a stainless-steel tube-in-tube reactor and subjected to catalytic ammonia synthesis under a parallel flow of N_2 and H_2 (1 : 3) at variable temperatures (275, 325, 375, and 425 °C) and pressures up to 10 bar. This approach was designed to test the morphological and surface-area gain in Solv-Li_4NH, aiming to meet the growing demand for catalytic systems that operate efficiently under lower temperatures and pressures. Remarkably, the solvothermal Li–N–H system demonstrated superior catalytic performance compared to hand-ground Li_4NH. At 275 °C and 1.25 bar, Solv-Li-N-H achieved an impressive ammonia production rate of 3.53 mmol g^{-1} h^{-1}, significantly higher than the 1.20 mmol g^{-1} h^{-1} rate exhibited by HG-Li_4NH at 325 °C (no substantial activity was detected for HG-Li_4NH at 275 °C). The gain in surface area and stability is further evidenced upon comparing Solv-Li_4NH with a ball-milled solid-state synthesized sample (BM-Li_4NH, ball-milled for 4 hours) which delivered the highest ammonia production rate of 3.690 mmol g^{-1} h^{-1} at 275 °C. However, its activity declined sharply, by 20.73% with

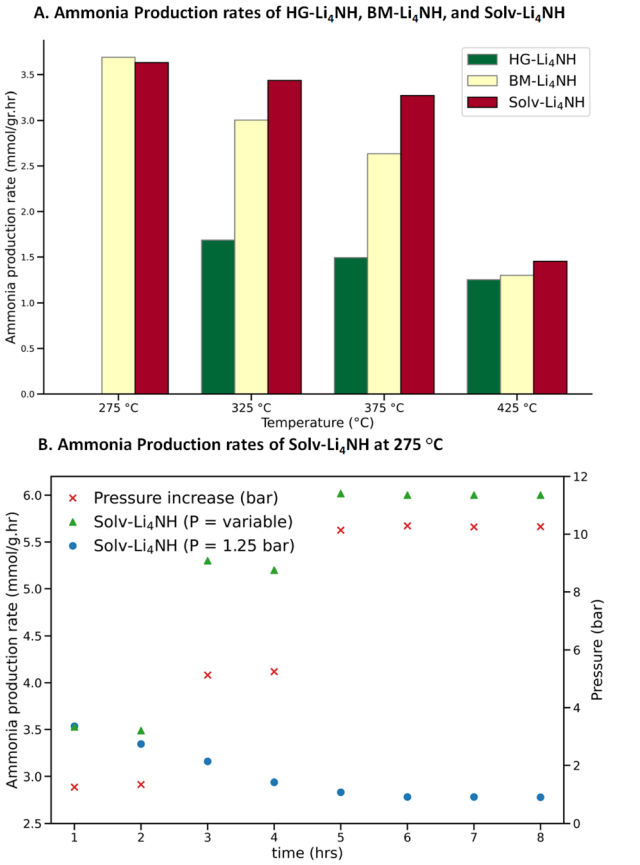

Fig. 5 Key metrics in ammonia synthesis (A) production rates of HG-Li_4NH, BM-Li_4NH, and Solv-Li–N–H systems at variable temperatures and 1.25 bar (B) production rates of Solv-Li–N–H system at 275 °C and variable pressures.

only a 50 °C increase in temperature, highlighting its temperature sensitivity (Fig. 5A). In contrast, the Solv-Li_4NH sample maintained notable stability, with just a 2.78% decrease under the same conditions. SEM images corroborate this behavior where BM-Li_4NH and HG-Li_4NH exhibit extensive particle coalescence after catalysis, obscuring and depleting active sites, whereas the Solv-Li_4NH preserves its nanoscale structure, ensuring greater resilience and sustained accessibility of active sites (Fig. SI-8).

Ammonia production decreases for all samples as the temperature exceeds 375 °C, and by 400 °C the rates converge to those of HG-Li_4NH and LiH. XRD of the post-catalytic samples confirms the predominance of LiH, with minor Li_2O, validating that at elevated temperatures the LiH-mediated regime dominates. Additionally, PXRD of the Solv-Li_4NH system distinctly reveals the presence of Li_2NCN phase, a signature of carbon contamination, which directly impacts catalytic stability. At 275 °C and 2 bar, the Solv-Li_4NH achieves an initial rate of 3.596 mmol g^{-1} h^{-1}, but this declines to 2.823 mmol g^{-1} h^{-1} within 4 h as the carbon is depleted, after which the rate levels off (22.7% activity loss consistent with 23.2 wt% Li_2NCN deactivation). Under 10 bar and 275 °C, the maximum production surpasses that of Co@Li_4NH at 450 °C and levels off at 6.01 mmol g^{-1} h^{-1}, further highlighting its enhanced low–temperature activity despite partial deactivation (Fig. 5B).

The origin of carbonaceous byproducts lies in solvent decomposition, a well-known limitation in solvothermal synthesis (*e.g.*, Mazumder *et al.* noted carbon charring in Ta_3N_5 starting from $TaCl_5$ and $LiNH_2$ in benzene at 500 °C).[13] In our case, the extent of decomposition strongly depends on solvent and reaction conditions. Although solvothermal samples prepared in benzene and toluene display comparable morphologies exposing a higher surface-to-volume ratio which ensures more accessible Li sites for N_2 activation and hydrogen transfer, the benzene sample exhibits more severe contamination, reflected in higher Li_2NCN content and a delayed N_2 uptake onset of 365 °C (Fig. SI-9). Longer synthesis durations exacerbate this effect as noted in the 48 h sample which progresses to over 90% deactivation, whereas the lowest contamination was obtained with the 12 h samples in dry toluene (traces of O_2 and H_2O intensify decomposition as well). Overall, while moderate Li_2NCN formation can transiently lower reactivity, excessive levels are detrimental, delaying the onset and reducing the extent of N_2 uptake. Toluene strikes a more favorable balance between morphology and contamination, which explains why its products consistently outperform the benzene-derived analogues in nitrogen fixation performance. Moreover, it is important to highlight the significant contribution of Li–N–H species in a catalytic role to the decomposition of hydrocarbon solvents; that is, conducting experiments with a blank system (toluene at 275 °C for 12 h) and a Ca–N–H system (calcium nitride Ca_3N_2 and calcium hydride CaH_2 at 275 °C for 24 h), showed no obvious evidence of solvent decomposition. Current work is therefore focused on minimizing carbon contamination through strategic solvent design and suppressing the LiH-dominated catalytic pathway by fully exploiting the *in situ* doping solvothermal route.

Promoting reaction progress and nanostructurisation. Despite these promising early results, one of the key challenges in these solvothermal systems resides in promoting reaction progress and rapid nucleation at relatively lower temperatures while modulating the growth of Li–N–H materials. That is, Li_4NH was successfully synthesized at 275 °C with partial dimensional control; nevertheless, none of the samples demonstrated complete reaction as residual phases were consistently observed indicating incomplete control over yield. Such control could be achieved *via* the incorporation of phase-directing additives and capping agents or mineralizers as they play a critical role in controlling solubility, nucleation, and crystallization.[38]

Herein, attempts to direct nucleation, growth and phase formation using conventional organic additives such as trioctylphosphine and triphenylphosphine did not yield discernible improvements in crystallinity, phase selectivity, or morphological control under the solvothermal conditions employed. For instance, while the addition of 20 mol% trioctylphosphine to toluene effectively narrows the size distribution, it simultaneously reduces solubility (and yield), promoting the growth of larger particles (Fig. SI-10). Indeed, phosphines appear to interact well with lithium-based precursors, potentially stabilizing them and mitigating solvent decomposition (Fig. SI-11 depicts reduced carbonaceous side products compared to SI-10 *via* extensive drying of TOP prior to use), but their limited efficacy arises from unfavorable solubility characteristics that hinder effective mediation of the solution-phase equilibria which impedes nucleation and favors growth. Amine additives such as urea, oleylamine, diethylenetriamine, and tetramethylethylenediamine simply yielded Li_2NCN (a precursor in the synthesis of various metal cyanamides[39]) due to lithium's thermodynamically favored decomposition of carbonaceous material to Li_2NCN (Fig. SI-12) and further hindered the progression of the reaction.

Mineralizers offer another route to influence behavior in solvothermal systems (in the following experiments, additives were introduced into toluene). The addition of lithium hexafluorophosphate ($LiPF_6$, 20 mol%) led to the preferential formation of LiF as a dominant phase (Fig. SI-13). In contrast, the inclusion of lithium halides, specifically lithium fluoride (LiF, 20 mol%) and lithium chloride (LiCl, 20 mol%), did not significantly alter the primary product formation but instead promoted the appearance of lithium nitride hydride and lithium nitride chloride mixtures. Similarly, the use of a eutectic LiCl–KCl mixture and LiCl–KCl mixture in toluene resulted in the formation of lithium nitride chloride as a byproduct (Fig. SI-14). This highlights a challenging feature of Li–N–H materials: their ability to incorporate various ions (*e.g.*, transition metals, metalloids, halides, *etc.*)[40] into their crystal structure, thus restricting the use of conventional salts and eutectic solvents.

Sodium amide as nanostructurisation promotor. Group I amides are occasionally employed as mineralizers in the synthesis of metal nitrides due to their strong basicity and ability to promote nitridation. In this work, sodium amide ($NaNH_2$) was selected primarily because of its low melting point

(210 °C) and thermal stability below its decomposition temperature (400 °C), which renders it well-suited as a molten phase/co-solvent under our solvothermal conditions. This behavior mimics aspects of hybrid molten salt synthesis, facilitating enhanced mass transport and precursor diffusion during reaction.

In our modified solvent-molten salt system, ball-milled Li_3N and LiH are suspended in anhydrous toluene containing $NaNH_2$ (5–20 wt%) and heated to a temperature range of 240–275 °C (Fig. SI-15). Even when used in small percentages, $NaNH_2$ altered the reaction pathway and composition of the expected Li–N–H phases, instigating the preferential appearance of sodium-doped Li–N–H $Fm\bar{3}m$ phase. Notably, with just 5 wt% of $NaNH_2$, the Li_3N conversion remains incomplete under solvothermal conditions, whereas incorporating 10 wt% or more drives the formation of the $Fm\bar{3}m$ phase and allows complete depletion of Li_3N at relatively lower temperatures (Fig. 6A), underscoring the essential role of $NaNH_2$ in lowering the reaction threshold and promoting phase transformation. The $Fm\bar{3}m$ phases obtained from the lower wt% presented variable lattice parameters all of which are in the vicinity of 4.99 Å, a nitride hydride rich composition. Rietveld refinement of the XRD data revealed a better fit when the $Fm\bar{3}m$ phase is fitted with two distinct lattice parameters; for instance, XRD data of the 10 wt% addition of $NaNH_2$ ($x = 0.10$) depicted an $Fm\bar{3}m$ phase with lattice parameters $a = 4.9848(11)$ and 5.0039(5) Å suggestive of compositional inhomogeneity within the sample. Furthermore, the disappearance of Na from the reaction mixture alludes to its incorporation into the crystal structure of a novel Li–Na–N–H $Fm\bar{3}m$ solid solution. Fig. 6B depicts the same reaction by the solid-state method, where a mixed product is observed including Na metal residue, tetragonal $I4_1/a$ Li_4NH phase and low percentages of the disordered $Fm\bar{3}m$ phase with lattice parameters $a = 4.9636(4)$ Å, with little indication of Na incorporation into the Li–N–H phases. This implies the potential for reaction pathway differentiation *via* the solvothermal approach.[41]

To better understand the mechanism and the role of $NaNH_2$ in driving the reaction into the $Fm\bar{3}m$ phase, the solvothermal reaction of a true hybrid molten-salt synthesis of 1 : 1 : 1 ratio of Li_3N, LiH and $NaNH_2$ was investigated. Rietveld refinement of synchrotron diffraction data of the Li_3N : LiH : $NaNH_2$ solvothermal system reveals the presence of a lithium imide-rich $Fm\bar{3}m$ phase ($a = 5.0272(0)$ Å) and a sodium hydride (NaH) $Fm\bar{3}m$ phase ($a = 4.8762(0)$ Å) (Fig. 7). The appearance of NaH in the system hypothesizes a stepwise reaction mechanism where metathesis of $NaNH_2$ and LiH yields $LiNH_2$ and NaH followed by the reaction of Li_3N and $LiNH_2$ (eqn (5) and (6)) to yield the imide. Indeed, at 5, 10, and 20 wt% $NaNH_2$, we postulate that metathesis with LiH is insufficient and LiH residue is thus noted while upon the equimolar addition of $NaNH_2$; LiH is fully consumed even at lower temperatures alluding to $NaNH_2$'s role in driving the reaction through an intermediate metathesis step. Note that metathesis between hydrides and group I amides, such as the MgH_2–$LiNH_2$ system, have been reported through solid-state approaches as an intermediary step during hydrogen release.[42,43] Thus, $NaNH_2$ was not subjected to ball milling with the precursor mixture as it would compromise this molten-mediated pathway (Fig. SI-16 depicts the Rietveld refinement of a ball-milled mixture of Li_3N, LiH, and $NaNH_2$ evidencing metathesis).

Herein, we highlight the capacity of the solvothermal approach to relatively stabilize mixed $Fm\bar{3}m$ phases incorporating heteroatoms up to a certain percentage; that is, prevent the decomposition of $NaNH_2$ into sodium metal by

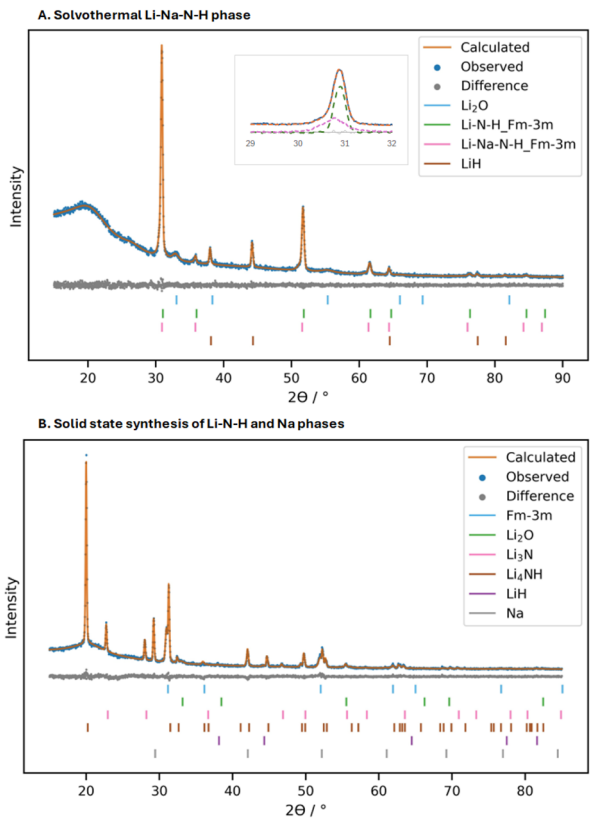

Fig. 6 Comparison of Rietveld refinement profiles for products synthesized with $NaNH_2$ at 275 °C *via* (A) the solvothermal route and (B) the conventional solid-state route.

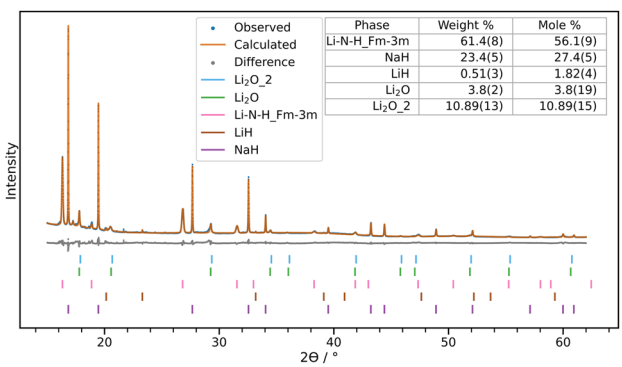

Phase	Weight %	Mole %
Li-N-H_Fm-3m	61.4(8)	56.1(9)
NaH	23.4(5)	27.4(5)
LiH	0.51(3)	1.82(4)
Li_2O	3.8(2)	3.8(19)
Li_2O_2	10.89(13)	10.89(15)

Fig. 7 Observed-calculated-difference (OCD) profile plot from the I-11 Rietveld refinement of the solvothermal $Fm\bar{3}m$ Li–N–H and NaH phases, note that the increased percentages of Li_2O_2 is attributed to exposure during sample transportation.

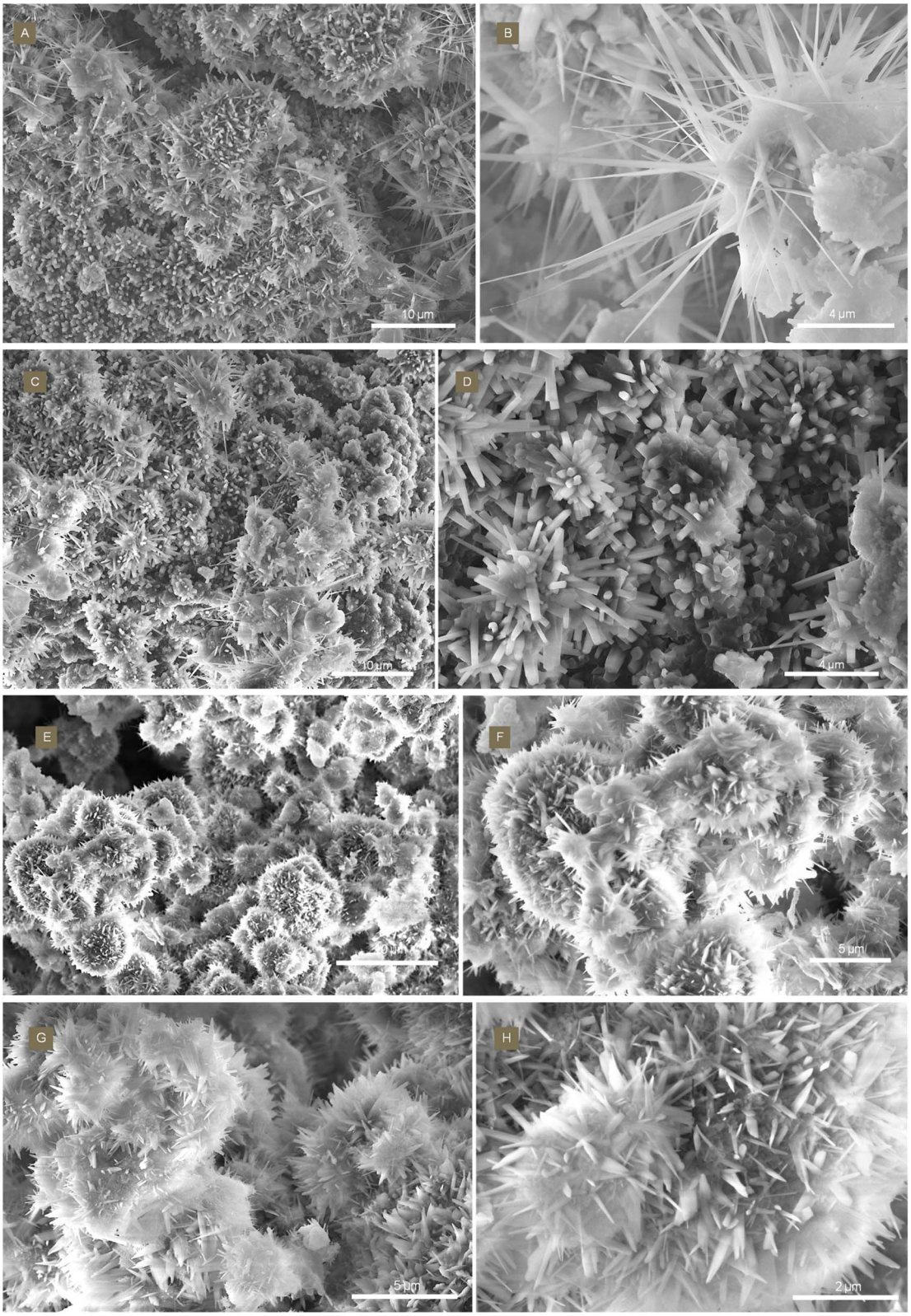

Fig. 8 Scanning electron microscopy (SEM) images of the solvothermal output of Li_3N, LiH and $xNaNH_2$ depicting (A–D) nanostructured needle-like and nanorods of the cubic $Fm\bar{3}m$ Li–Na–N–H phase ($x = 0.2$) and (E–F) needle-like nanostructured composites of Li–N–H and NaH materials.

incorporating Na^+ within $Fm\bar{3}m$ crystal structure as opposed to the lack of intercalation noted in SS synthesis. Hence, the presence of $NaNH_2$ in the system introduces Na^+ species into the Li–N–H lattice, facilitating defect formation and enhanced ion mobility. The results are consistent with the solid-state doping of Li_2NH with LiH which yielded a non-stoichiometric imide-hydride solid solution.[44] Ongoing synchrotron investigations are being conducted to elucidate the definitive reaction mechanism and track the structural dynamics of the intermediate phases in the solvothermal and solid-state approaches. This integration of sodium emphasises the significance of the solvothermal synthetic approach particularly as it could be extended to incorporate various critical hetero ions, such as potassium, calcium, and an array of transition metals, which are often regarded as N_2 and H_2 dissociation promotors in the catalyzed ammonia production process.

$$LiH + NaNH_2 \rightarrow LiNH_2 + NaH \quad (5)$$

$$Li_3N + LiNH_2 \rightarrow Fm\bar{3}m\text{-}Li_2NH \quad (6)$$

SEM images of the solvothermal Li and Na mixed phases reveal a semi-uniform low- and high-aspect ratio distribution of particle sizes and morphologies that varies with the percentage of $NaNH_2$ added. In a hybrid molten-solvent system comprising 5 wt% and 10 wt% of $NaNH_2$, meso-quasi-spherical particles can be noted ranging from 100 to 600 nm and large aggregates of 1.6 μm with nanowires noted sporadically for the 10 wt% sample (Fig. SI-17) as opposed to the pseudo-spherical morphology of the lithium nitride hydride system. At ≥20 wt% $NaNH_2$, large aggregates composed of needle-like and nanowire morphologies are observed throughout the sample with sizes of individual needles and wires ranging from 300 to 900 nm and large aggregates ranging from 1 to 6 μm (Fig. 8). These data imply that as $NaNH_2$ increases, it induces a significant increase in the mobility of Li^+, Na^+, NH_2^-, $N^{3-}$and H^- species and allows for rapid and preferential addition of building blocks *via* adsorption onto facets of the growing nuclei. This differential adsorption lowers the surface energy of side facets and promotes elongation into needles and wires. Such nanostructures are absent in the analogous SS reactions where all samples display irregular and non-uniform morphologies consistent with bulk metallic/metallic oxide nitride alloys (Fig. SI-18).

The N_2 uptake profiles of solvothermal samples reveal the advantages of nanostructuring where the 20 wt% $NaNH_2$ sample exhibits earlier onset of reactivity and higher nitrogen uptake per unit mass compared to 10 wt% of $NaNH_2$, despite a higher level of carbon contamination in the 20 wt% sample whereas the 1 : 1 : 1 sample displays a delayed onset due to the higher carbon contamination which instigates the irreversible formation of Li_2NCN (Fig. 9A). That is, as $NaNH_2$ content increases so does carbon contamination (indicative of $NaNH_2$'s role in promoting solvent decomposition) which in turn induces a marked decline in activity due to deactivation resulting from the formation of Li_2NCN. An in-depth investigation into the mass spectrometry coupled with TGA for the 1 : 1 : 1 sample confirms that hydrogen evolution accompanies mass loss associated with Li_2NCN formation (Fig. 9B). Notably, mass loss begins at 100 °C for the 1 : 1 : 1 sample, 125 °C for the 20 wt% sample, 200 °C for the 10 wt% sample and 225 °C for Solv-Li_4NH and further exhibits NH_3 evolution between 350 and 450 °C due to the *in situ* H_2 evolution and N_2 atmosphere. The volatile gases, absent in the Solv-Li_4NH sample, indicate both thermodynamic and kinetic gains from nanostructurisation, for all occurring reactions (Li_2NCN formation, N_2-uptake, and *in situ* NH_3 synthesis).

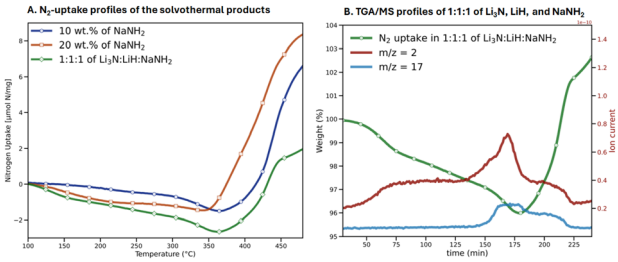

Fig. 9 N_2 uptake profiles as measured in a TPR experiment of (A) 10, 20 wt% and equimolar addition of $NaNH_2$ and (B) N_2 uptake and gas evolution of 1 : 1 : 1 of Li_3N : LiH : $NaNH_2$ (ramp to 500 °C followed by 60 min isothermal segment).

Extension to other M-N-H systems. Building on the promising results obtained with the Li–N–H system, the method has been systematically extended to other Group I and Group II M-N-H materials, which are of particular interest due to their emerging catalytic activity and/or promotion effects.[5,45] For instance, the validity of the synthetic protocol was established for stochiometric lithium imide Li_2NH where the solvothermal reaction of Li_3N and $LiNH_2$ proceeds entirely into the $Fd\bar{3}m$ phase at 205 °C and transitions successively to the $Fm\bar{3}m$ with temperature increase (Fig. SI-19). $Li_3Na(NH_2)_4$ has also been isolated with morphological uniqueness (Fig. SI-20). The reaction of calcium nitride Ca_3N_2 and calcium hydride CaH_2 at 275 °C forms a mixture of $Fd\bar{3}m$ calcium nitride hydride and $Fm\bar{3}m$ calcium imide CaNH phases in 57% yield (Fig. SI-21). Notably, no traces of calcium carbide (CaC_2) or calcium carbodiimide were detected, indicating diminished or absence of solvent decomposition; further optimization of reaction parameters is currently under investigation for the isolation of uniformly nanostructured nitride hydride and imide phases.

Conclusion

The development of soft chemistry synthesis routes of Li–N–H materials is driven by the need to engineer nanoscale systems with pronounced activity in green energy and catalysis. Li_4NH and lithium imide–nitride hydride solid solutions, in addition to Na-doped Li–N–H phases were successfully synthesized through a solvothermal route starting from commercially available precursors. The solvothermally synthesized samples display unique morphologies that cannot be accessed by conventional solid-state methods. The Li–N–H systems showed more uniform and smaller particle sizes when synthesized

solvothermally, removing the need for an additional mechanochemical treatment as would be required for solid state synthesized samples. The approach enables a NH_3 production rate of up to 6 mmol h^{-1} per gram of the sample surpassing reported activity of transition metal composited Li_4NH despite 23 wt% deactivation *via* Li_2NCN. Further optimization of the solvent system and reaction conditions is under investigation to fine-tune the reaction mixture and avoid the possibility of considerable carbon contamination originating from solvent decomposition. The addition of a sodium amide mineralizer demonstrated the ability to form dramatically altered morphologies, including the formation of nanoneedles and nanorods. While more control is imperative, the method provides proof of concept of the plausible nano-synthesis methods of materials associated with the Li–N–H family, evidenced by the Li/Na nanostructured systems, thereby paving the way for further investigations into sophisticated and intricate nanostructurisation techniques and their implications on the mechanism of action of these systems in catalysis, hydrogen storage, solid-state electrolytes and Li-ion batteries.

Conflicts of interest

There are no conflicts to declare.

Data availability

Data for this article, including raw XRD and TGA data are available at UBIRA eData at **https://doi.org/10.25500/edata.bham.00001362**.

Supplementary information is available. See DOI: **https://doi.org/10.1039/d5ta04960a**.

Acknowledgements

This project has received funding from the European Union's Horizon 2020 research and innovation program under Grant Agreement No. 101058565 (AMBHER project). JWM acknowledges a UKRI Future Leaders Fellowship (MR/Y00387X/1). Diamond Light Source is acknowledged for the provision of beamtime (CY29996-1).

Notes and references

1 M. D. Allendorf, V. Stavila, J. L. Snider, M. Witman, M. E. Bowden, K. Brooks, B. L. Tran and T. Autrey, *Nat. Chem.*, 2022, **14**, 1214–1223.
2 H. Wang, X. Liang, J. Wang, S. Jiao and D. Xue, *Nanoscale*, 2020, **12**, 14–42.
3 J. L. White, A. A. Baker, M. A. Marcus, J. L. Snider, T. C. Wang, J. R. I. Lee, D. A. L. Kilcoyne, M. D. Allendorf, V. Stavila and F. El Gabaly, *Adv. Mater. Interfaces*, 2020, **7**, 1901905.
4 G. J. Irvine, R. I. Smith, M. O. Jones and J. T. S. Irvine, *Nat. Commun.*, 2023, **14**, 4389.
5 Y. Guan, W. Zhang, Q. Wang, C. Weidenthaler, A. Wu, W. Gao, Q. Pei, H. Yan, J. Cui, H. Wu, S. Feng, R. Wang, H. Cao, X. Ju, L. Liu, T. He, J. Guo and P. Chen, *Chem Catal.*, 2021, **1**, 1042–1054.
6 M. Kitano, Y. Inoue, M. Sasase, K. Kishida, Y. Kobayashi, K. Nishiyama, T. Tada, S. Kawamura, T. Yokoyama, M. Hara and H. Hosono, *Angew. Chem., Int. Ed.*, 2018, **57**, 2648–2652.
7 C. Brooker-Davis, J. Makepeace and T. Wood, *J. Ammon. Energy*, 2023, **1**(1), 46–58.
8 T. J. Wood, J. W. Makepeace and W. I. F. David, *Phys. Chem. Chem. Phys.*, 2017, **19**, 27859–27865.
9 J. P. Lowen, T. Insinna, T. V. Beatriceveena, M. P. Stockham, B. Dong, S. J. Day, C. P. Grey, E. Kendrick, P. R. Slater, P. A. Anderson and J. W. Makepeace, *EES Batteries*, 2025, **1**, 527–540.
10 J. Wang, G. Lei, T. He, H. Cao and P. Chen, *J. Energy Chem.*, 2022, **69**, 555–560.
11 M. Fang, G. Dong, R. Wei and J. C. Ho, *Adv. Energy Mater.*, 2017, **7**, 1700559.
12 G. Demazeau, *J. Mater. Sci.*, 2008, **43**, 2104–2114.
13 B. Mazumder, P. Chirico and A. L. Hector, *Inorg. Chem.*, 2008, **47**, 9684–9690.
14 D. Bokov, A. Turki Jalil, S. Chupradit, W. Suksatan, M. Javed Ansari, I. H. Shewael, G. H. Valiev and E. Kianfar, *Adv. Mater. Sci. Eng.*, 2021, **2021**, 5102014.
15 M. A. Boles, M. Engel and D. V. Talapin, *Chem. Rev.*, 2016, **116**, 11220–11289.
16 T. Klein and G. Kickelbick, *Dalton Trans.*, 2020, **49**, 9820–9834.
17 A. Schneemann, J. L. White, S. Kang, S. Jeong, L. F. Wan, E. S. Cho, T. W. Heo, D. Prendergast, J. J. Urban, B. C. Wood, M. D. Allendorf and V. Stavila, *Chem. Rev.*, 2018, **118**, 10775–10839.
18 M. J. Lee, J. Han, K. Lee, Y. J. Lee, B. G. Kim, K.-N. Jung, B. J. Kim and S. W. Lee, *Nature*, 2022, **601**, 217–222.
19 J. P. Lowen and J. W. Makepeace, *ECS Meeting Abstracts*, 2022, MA2022-01, 553.
20 M. Hirscher, V. A. Yartys, M. Baricco, J. Bellosta von Colbe, D. Blanchard, R. C. Bowman, D. P. Broom, C. E. Buckley, F. Chang, P. Chen, Y. W. Cho, J.-C. Crivello, F. Cuevas, W. I. F. David, P. E. de Jongh, R. V. Denys, M. Dornheim, M. Felderhoff, Y. Filinchuk, G. E. Froudakis, D. M. Grant, E. M. Gray, B. C. Hauback, T. He, T. D. Humphries, T. R. Jensen, S. Kim, Y. Kojima, M. Latroche, H.-W. Li, M. V. Lototskyy, J. W. Makepeace, K. T. Møller, L. Naheed, P. Ngene, D. Noréus, M. M. Nygård, S.-i. Orimo, M. Paskevicius, L. Pasquini, D. B. Ravnsbæk, M. Veronica Sofianos, T. J. Udovic, T. Vegge, G. S. Walker, C. J. Webb, C. Weidenthaler and C. Zlotea, *J. Alloys Compd.*, 2020, **827**, 153548.
21 J. W. Makepeace, M. O. Jones, S. K. Callear, P. P. Edwards and W. I. F. David, *Phys. Chem. Chem. Phys.*, 2014, **16**, 4061–4070.
22 Q. Cheng, A. Muhammad, O. Kaario, Z. Ahmad and L. Martti, *Renewable Sustainable Energy Rev.*, 2025, **207**, 114995.
23 J. W. Makepeace, J. M. Brittain, A. S. Manghnani, C. A. Murray, T. J. Wood and W. I. David, *Phys. Chem. Chem. Phys.*, 2021, **23**, 15091–15100.

24 T. Ichikawa, S. Isobe, N. Hanada and H. Fujii, *J. Alloys Compd.*, 2004, **365**, 271–276.
25 M. Ravi and J. W. Makepeace, *Chem. Commun.*, 2022, **58**, 6076–6079.
26 M. Ravi and J. W. Makepeace, *Chem. Sci.*, 2022, **13**, 890–908.
27 N. Tapia-Ruiz, A. G. Gordon, C. M. Jewell, H. K. Edwards, C. W. Dunnill, J. M. Blackman, C. P. Snape, P. D. Brown, I. MacLaren and M. Baldoni, *Nat. Commun.*, 2020, **11**, 4492.
28 N. Scotti, F. Flacke, R. Ludwig and H. Jacobs, *Z. Anorg. Allg. Chem.*, 1998, **624**, 1395–1399.
29 H. Jacobs and B. Harbrecht, *Z. Anorg. Allg. Chem.*, 1984, **518**, 87–100.
30 H. Jacobs and B. Harbrecht, *J. Less-Common Met.*, 1982, **85**, 87–95.
31 V. S. Marakatti and E. M. Gaigneaux, *ChemCatChem*, 2020, **12**, 5838–5857.
32 R. Marx, *Z. Anorg. Allg. Chem.*, 1997, **623**, 1912–1916.
33 N. Tapia-Ruiz, N. Sorbie, N. Vaché, T. K. A. Hoang and D. H. Gregory, *Materials*, 2013, **6**, 5410–5426.
34 J. W. Makepeace, T. J. Wood, H. M. A. Hunter, M. O. Jones and W. I. F. David, *Chem. Sci.*, 2015, **6**, 3805–3815.
35 J. W. Makepeace, J. M. Brittain, A. Sukhwani Manghnani, C. A. Murray, T. J. Wood and W. I. F. David, *Phys. Chem. Chem. Phys.*, 2021, **23**, 15091–15100.
36 J. Zhang and Y. H. Hu, *Ind. Eng. Chem. Res.*, 2011, **50**, 8058–8064.
37 L. Liu, F. Lu, J. Tian, S. Xia and Y. Diao, *Appl. Phys. A*, 2019, **125**, 366.
38 J. Lai, W. Niu, R. Luque and G. Xu, *Nano Today*, 2015, **10**, 240–267.
39 P. Schneiderhan, E. Bayat, M. Ströbele, D. Enseling, T. Jüstel and H. J. Meyer, *Dalton Trans.*, 2025, **54**, 4909–4917.
40 W. Li, M. Li, P.-H. Chien, S. Wang, C. Yu, G. King, Y. Hu, Q. Xiao, M. Shakouri, R. Feng, B. Fu, H. Abdolvand, A. Fraser, R. Li, Y. Huang, J. Liu, Y. Mo, T.-K. Sham and X. Sun, *Sci. Adv.*, 2023, **9**, eadh4626.
41 F. Abi-Ghaida and J. Makepeace, 2025.
42 J. J. Hu, E. Röhm and M. Fichtner, *Acta Mater.*, 2011, **59**, 5821–5831.
43 D. Pottmaier, F. Dolci, M. Orlova, G. Vaughan, M. Fichtner, W. Lohstroh and M. Baricco, *J. Alloys Compd.*, 2011, **509**, S719–S723.
44 E. Fee, *Influence of Hydride Doping of Lithium Imide on the Electrochemical Properties for Solid State Electrolyte Development*, University of Birmingham, 2025.
45 X. Fu, V. A. Niemann, Y. Zhou, S. Li, K. Zhang, J. B. Pedersen, M. Saccoccio, S. Z. Andersen, K. Enemark-Rasmussen, P. Benedek, A. Xu, N. H. Deissler, J. B. V. Mygind, A. C. Nielander, J. Kibsgaard, P. C. K. Vesborg, J. K. Nørskov, T. F. Jaramillo and I. Chorkendorff, *Nat. Mater.*, 2024, **23**, 101–107.